Towards Multidisciplinary Wind Turbine Design using High-Fidelity Methods

Manfred Imiela[1] and Felix Wienke[2]
DLR, German Aerospace Center

and

Christoph Rautmann[3], Christian Willberg[4], Philipp Hilmer[5] and Alexander Krumme[6]
DLR, German Aerospace Center

Reliable predictions for wind turbines become more and more difficult with the increase in overall size and weight. On the one hand external factors such as the influence of wind shear become more important for bigger turbines, internal factors such as structural layout and challenges in the manufacturing process need to be addressed on the other hand. Accurate aerodynamic simulations are an essential requirement for further analyses of aeroelastic stability and aeroacoustic footprint. While the calculations in all of these individual disciplines are challenging the combined simulation of all these disciplines, namely the multidisciplinary simulation is a tough but gainful undertaking. This task is being addressed in the DLR project MERWind which will be presented here. The focus of the paper lays on the aerodynamic and aeroelastic simulation of the NREL 5MW wind turbine using high-fidelity methods.

Nomenclature

α = shaft angle [°]
β = precone angle [°]
κ = von Kármán constant
ψ = azimuth angle [°]
ω = turbulent dissipation rate [1/s]
c_P = pressure coefficient, $(P-P_\infty)/(0.5\rho_\infty v_{tip}^2)$
C_μ = k-ω model constant, $C_\mu = 0.09$
D = diameter
$\vec{F}$ = force vector [N]
F_x = thrust force [N]
k = turbulent kinetic energy [m²/s]
k_r = equivalent sand grain roughness [m]
M_x = shaft torque [Nm]
$\vec{M}$ = moment vector [Nm]
$\vec{r}_{nk}$ = displacement vector from k relative to n
R = rotor radius [m]
u = streamwise velocity [m/s]
u_τ = friction velocity [m/s]
v_{tip} = blade tip velocity [m/s]
x = streamwise coordinate
y = transverse coordinate
z = vertical coordinate normal to ground
z_{ref} = reference height [m]
z_0 = roughness length [m]
BLP = boundary layer profile

I. Introduction

Over the last decade the size of wind turbines has substantially increased. Currently this trend seems to continue in order to reach the ambitious goals which have been set for energy production from renewable sources, especially wind energy. Increasing hub heights and blade lengths will require major technological improvements. A

[1] Research Scientist, Institute of Aerodynamics and Flow Technology, Lilienthalplatz 7, Braunschweig.
[2] Research Scientist, Institute of Aeroelasticity, Bunsenstraße 10, Göttingen.
[3] Research Scientist, Institute of Aerodynamics and Flow Technology, Lilienthalplatz 7, Braunschweig.
[4] Research Scientist, Institute of Composite Structures and Adaptive Systems, Lilienthalplatz 7, Braunschweig.
[5] Research Scientist, Institute of Composite Structures and Adaptive Systems, Lilienthalplatz 7, Braunschweig.
[6] Research Scientist, Institute of Propulsion Technology, Bunsenstraße 10, Göttingen.

key element for advancements in the wind energy business will be accurate simulation methods taking into account the multidisciplinary nature of wind turbines. In the industrial context up to now simple methods based on the blade element momentum theory are still widely used for aerodynamic predictions due to their low turn-around times. Despite the fact that computational fluid dynamic (CFD) methods are still too time-consuming to be used within the certification process, the evaluation of a few dozen designs and the subsequent comparison becomes feasible. From this analysis valuable information on the effect of the investigated design parameters can be deduced.

In the scientific area CFD methods have already been applied for several years. Some pioneering work can be found in Hansen[1] et al. giving a comprehensive overview on the various methods from simple BEM over panel methods to CFD methods even including aeroelasticity. In the beginning a lot of publications focused on simulating model scale rotors which have been investigated in wind tunnel experiments in order to compare with the experimental results. Extensive research has for example been done on the NREL Phase VI rotor. Sorensen[2] et al. compare simulated results achieved with the incompressible CFD solver EllipSys3D to the experimental values and obtain good agreement for non-separated flow cases. Five years later Sorensen[3] et al. present the simulation of the UPWIND rotor under sheared inflow conditions showing the effect on thrust and mechanical power output. Another valuable research on the simulation of a model rotor was undertaken by Meister[4] et al. using the compressible CFD Solver FLOWer to investigate the flow field around the Mexico turbine.

In order to account for the effect of turbulence and to simulate state of the art rotor sizes Troldborg[5] et al. present the simulation of the NREL 5MW turbine also prescribing turbulent inflow. Another recent work on the NREL 5MW is presented by Yu[19] et al. using CFD-CSD coupled computations.

II. MERWind – Multidisciplinary Design and Analysis Framework for Wind Turbines

A. General Setup

The MERWind project aims at developing a design and analysis framework which enables the integrated simulation of wind turbines with respect to aerodynamics, structure, aeroelasticity, aeroacoustics and manufacturing aspects. For this purpose already existing codes from each discipline are embedded in an optimization environment. as depicted in Fig. 1. The aerodynamic analysis (upper level) of the current multidisciplinary design cycle is performed using the DLR's CFD-code TAU[6]. The resulting aerodynamic loads are passed on to the structural model (lower level) where the sizing is carried out using the preprocessor Hypersizer[7] and the FEM program Ansys Structural. An internal optimization process minimizes the structural weight while assuring structural integrity. Once an adequate structural blade design has been found the FEM model is integrated into the multibody program SIMPACK[8] and the blade deformation according to the aerodynamic loading is calculated. The analysis process is terminated as soon as the deformation between two subsequent fluid-structure interactions reaches a predefined threshold. In this case the goal function is determined and communicated to the global process control (AutoOpti). Otherwise the next fluid-structure interaction cycle is started. After having evaluated a number of different designs AutoOpti[9] creates a response surface model from the inputs (design vector) and outputs (goal function) in order to perform a sensitivity analysis on the given design parameters. The CPACS[10] (Common Parametric Aircraft Configuration Scheme) data exchange format has been chosen for communication purposes between the different programs.

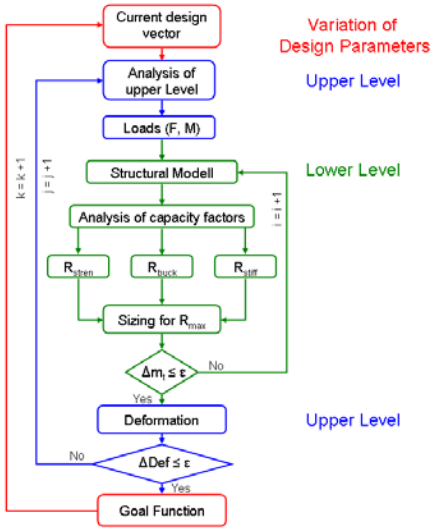

Fig. 1. Multilevel design process.

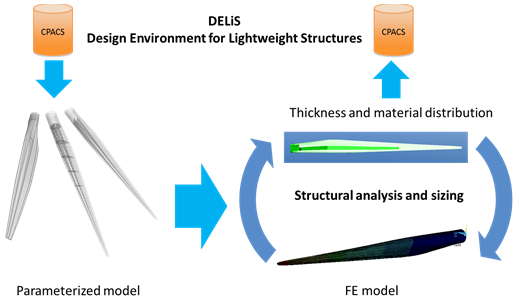

Fig. 2. Structural design process.

B. Structural Design

Fig. 2 illustrates the structural analysis and sizing process. The CPACS dataset is interpreted by the python-based software DELiS[7] which creates a parameterized model. Based on this model DELiS is able to generate a finite

element (FE) model. This FE-model is used to calculate displacements and stresses as response from the external loads. Subsequently the commercial software Hypersizer calculates the laminates and/or thicknesses for different regions and updates the FE-model. This process is iteratively repeated until the structure is sized with a minimum amount of weight. At the end the thickness and material distribution are written back to the CPACS dataset. Since the whole process is parameterized it is easily possible to study various blade designs.

C. Fluid-Structure-Interaction-Framework (FSI-Framework)

In the first step a parameterized CAD geometry is built using the commercial software CATIA V5 by extracting the relevant geometry information from the CPACS database. Subsequently the commercial mesh generator Pointwise is launched in order to create a structured mesh around the new blade geometry. The FSI-Framework consists of DLR's flow solver TAU and the Multibody-code SIMPACK. Both codes are coupled iteratively in a loose manner. Before the FSI-computation can be started the FE-model of the rotor blade from the structural design subprocess is incorporated into the SIMPACK model. Aerodynamic and aeroelastic calculations are carried out alternately until the FSI-process is converged. Afterwards global parameters such as power, forces and deformation of the rotor are transferred back to the CPCAS database. A more detailed description can be found in chapter 4.

D. Aeroacoustic Analysis

The main sound source of wind turbines is airframe noise. A reliable and efficient prediction capability for airframe noise problems is needed as a technology enabler to achieve further noise reduction. Fast simulations of broadband noise are conducted by means of sound sources from synthetic turbulence as depicted in Fig. 3. The Random Particle Method[11] is a synthetic turbulence generator that enables the generation of fluctuating sound sources from RANS, taking into account the major specifications that have to be realized to be appropriate for an application to aeroacoustic problems. The sound generation and radiation is simulated in non-uniform flow via forced acoustic perturbation equations using the Computational Aero Acoustics (CAA) code PIANO, developed at DLR. In order to reduce the computational cost, the CAA domain covers the outer blade part.

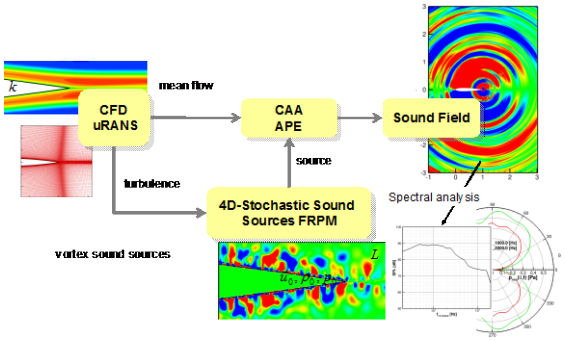

Fig. 3. Aeroacoustic analysis procedure.

The extrapolation to the farfield is done using the Ffowks-Williams Hawking (FW-H) method in a rotating frame of reference. The advantages of using this approach in contrast to LES or DNS lies in the computational time (around 3 orders of magnitude less) and it is based on a uRANS computation which is also needed for design purpose.

E. Manufacturing Aspects

An important part of an integrated design tool is the connection between aerodynamic dimensioning and structural design and the actually built rotor blade leaving the factory. The manufacturing process of a wind turbine blade traditionally incorporates a big amount of manual work even nowadays. Blade production is mainly cost driven and especially in countries with high average salaries cost reduction while ensuring high quality is a main driver. Therefore, it is highly desirable to know the connections between manufacturing and design, since severe tolerance requirements following high-fidelity aerodynamic design might result in a high financial effort that is not acceptable. On the other hand production might be able to show ways to substantially reduce costs by using new manufacturing technologies.

Fig. 4. Measuring campaign.

The goal of MERWind is the buildup of a bidirectional model that works from aerodynamic dimensioning through structural design to manufacturing costs as well as the other way round. Tolerances in the manufacturing process are recorded in various measuring campaigns as shown in Fig. 4 and are integrated into the cost model. This will help to identify possible benefits and drawbacks of new manufacturing technologies from a design point of view. In addition, the assessment of design from a production point of view will provide the ability to rate different designs against each other.

III. Aerodynamic Simulation

In this section only rigid CFD calculations are considered. The focus lies on the detailed comparison of different configurations and inflow conditions, while the coupled simulations are presented in chapter 4.

A. CFD Solver TAU

The TAU-Code[6] developed at the Institute of Aerodynamics and Flow Technology is used for the aerodynamic simulations. It solves the compressible, three-dimensional Reynolds-Averaged Navier-Stokes (RANS) equations using a finite volume formulation. The program consists of several modules that are integrated in the simulation environment FlowSimulator. This python-based framework performs the coupling between the different modules and allows in-memory data exchange. The following modules are contained within the TAU code:

- Preprocessor module: creates dual-grid and agglomeration levels for multi-grid
- Solver module: solves the flow equation on the dual-grid
- Motion module: handles relative motion of different chimera components
- Deformation module: applies deformation on solid bodies and propagates the deformation into the flow domain
- Adaptation module: grid refinement or coarsening according to special flow phenomena, e.g. shocks, etc.

The TAU-Code uses a cell-vertex formulation with a dual-grid approach for the spatial discretization. The solver module contains a central scheme as well as several upwind schemes for the discretization of the inviscid fluxes. Viscous terms are computed with a second-order central scheme. For artificial dissipation scalar or matrix dissipation might be chosen by the user. The unstructured code supports the use of hybrid meshes, i.e. mixed type of elements (hexaeder, tetraeder, etc.) offering more flexibility in the mesh generation process.

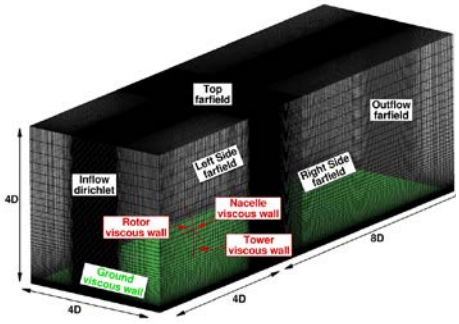

Fig. 5. Configuration A (rotor only) and Configuration B (complete turbine).

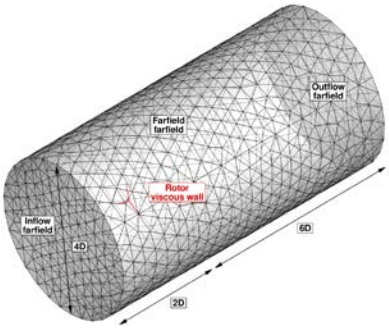

Fig. 6. Configuration C (rotor, steady computation).

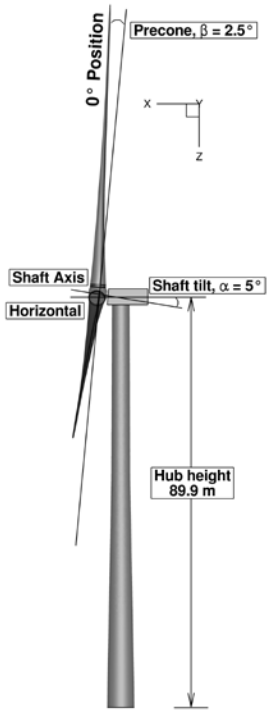

Fig. 7. NREL 5MW Reference Setup.

Time integration is achieved using either an explicit Runge-Kutta type time-stepping scheme or an implicit LU-SGS (lower-upper symmetric Gauss-Seidel) algorithm. The time-accurate simulations are performed with an implicit dual-time stepping approach. Various multi-grid type cycles are available for accelerating the convergence of the flow equations. For the pure aerodynamic calculations the LU-SGS scheme is used in combination with a 3w multi-grid cycle.

For the simulation of turbulent flows several one- and two-equation turbulence models are implemented. Here, the two-equation k-ω model of Wilcox is used in order to facilitate the reconstruction of synthetic turbulence for the acoustic analysis.

The simulation of stationary and rotating parts is accomplished by the motion module and the chimera technique[12]. While the motion module handles the relative motion of different parts the chimera technique allows the overlapping of meshes and performs the interpolation from one mesh to the other and therefore eases the mesh generation process. The motion can either be prescribed by a polynomial function or an external motion file provided by an external program.

B. Computational Setup

Three different mesh configurations are generated for the pure aerodynamic simulations. In all cases the NREL 5-MW turbine as defined by Jonkman et al.[13] serves as reference turbine (Fig. 7). At first the complete wind turbine

including tower, nacelle, hub, stubs and the three blades as depicted in Fig. 5 is regarded (configuration B). The turbine features a shaft angle (α) of 5° and a precone (β) of 2.5° as described in the reference document. Since the configuration will also be used for simulations of a boundary layer profile the background mesh features a high grid resolution in the vicinity of the ground. The decisive surfaces and their respective boundary condition are labelled in Fig. 5. The black surfaces indicate non-solid surfaces (farfield or dirichlet boundary condition), while the coloured surfaces mark solid walls (viscous wall).

The second setup (configuration A) only contains the rotor, hub and the stubs. Shaft angle and precone are also considered. Also the background mesh and the boundary conditions from the previous setup are kept in order to make the results directly comparable (tower and nacelle are filled with prisms and tetras to remove blocking effect).

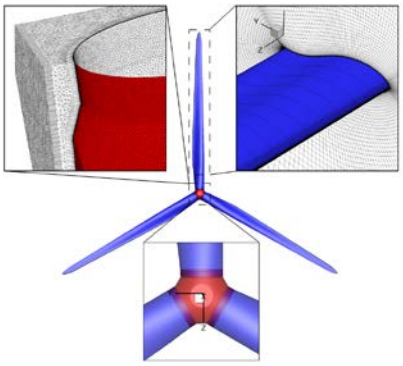

Fig. 8. Hub and blade mesh.

The third configuration as shown in Fig. 6 is used for steady simulations only and therefore does not include the shaft angle. In a first step only one third of the rotor and hub is meshed. Unfortunately the FlowSimulator does not support the calculation of periodic meshes at this time. Therefore subsequently the mesh is duplicated and rotated in order to get a complete rotor.

While the rotor for configuration C is modelled as one solid body, the rotor for configuration A and B consists of different parts, namely the hub, the stubs and the blades as depicted in Fig. 8. Also the high boundary layer resolution on the hub as well as on the blade can be seen. In average a first wall spacing of 3e-06 m was used to achieve y^+ values below one. The reader should also note the structured overlap region at the chimera boundary of the hub mesh which allows a very small gap between the nacelle and the rotor of about 10 cm.

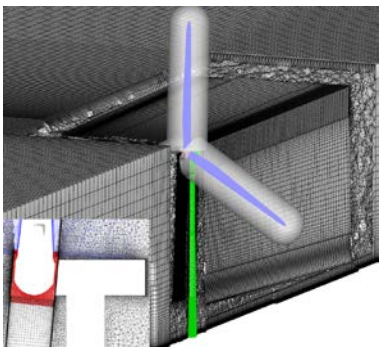

Fig. 9. Chimera Setup.

The complete mesh setup showing all chimera components and the overlap regions is depicted in Fig. 9. While the tower and the nacelle are placed in the stationary background grid (black grid), the hub and blade stubs (red grid) as well as the blades (blue grid) are discretized separately. While the blade meshes consist of pure hexahedra cells, the hub and the background mesh include also unstructured elements. In the background grid structured blocks are used behind the turbine in order to guarantee a good preservation of the tip vortex wake as can be seen in Fig. 9 since they allow for a better control of the grid resolution. The reader should note the widening of the structured area guaranteeing a good resolution of the wake as it is expanding downstream. Unstructured regions fill the gap between the highly resolved area and the coarser farfield.

Table 1. Inflow conditions for configuration A, B and C for uniform and BLP conditions.

Case	Uniform			BLP		
	Wind Speed	Rotor Speed	Pitch Angle	z_{ref}	z_0	κ
Rated	11.4 m/s	12.1 rpm	0°	100	0.01	0.41

On one hand modelling the components separately increases the complexity of the simulation since the blade surface from the hub and the blade have to overlap to obtain a watertight surface and to make the chimera interpolation feasible. On the other hand the simulation becomes more flexible when load cases with pitch adjustment have to be considered. In this case the blade can easily be rotated through the TAU motion module.

The inflow conditions for the different configurations are listed in Table 1. For configuration A and B uniform inflow conditions for the rated wind speed case are considered as well as a logarithmic boundary layer profile (BLP). The reason for this is that a real wind turbine is not exposed to a uniform inflow velocity but experiences velocities varying with height due to the earth's atmospheric boundary layer. According to Zhang[14] the earth's boundary layer is divided into four main areas: the laminar bottom layer, the Prandtl layer, the Ekman layer and the free atmosphere. Depending on the local conditions (most of all stratification due to thermal effects) the thickness of the Prandtl layer can vary between a few meters and more than 100m. For

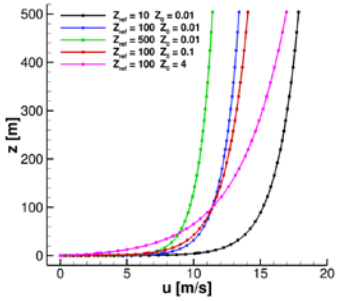

Fig. 10. BLP for various z_{ref} and z_0

simplification reasons we assume in this paper that the wind turbine is fully submerged in the Prandtl layer meaning that the shear stress is constant with height. The ground on which the wind turbine stands will be considered as aerodynamically rough representing the presence of grass, bushes, houses, etc. The velocity profile can then be described by equation (1) where z_0 is the roughness length describing the type of terrain. This is exactly the formula for rough surfaces implemented in the TAU code by Knopp[15] et al. In order to be consistent not only the streamwise velocity has to be modified but also the turbulent kinetic energy (k) and the turbulent dissipation (ω) have to be altered accordingly to equation (2) and equation (3) with the relation $z_0 = 0.03 * k_r$.

$$\frac{u}{u_\tau} = \frac{1}{\kappa} \ln\left(\frac{z + z_0}{z_0}\right) \quad (1)$$

$$k = \frac{u_\tau^2}{\sqrt{C_\mu}} \quad (2)$$

$$\omega = \frac{u_\tau}{\kappa \sqrt{C_\mu}(z + z_0)} \quad (3)$$

Since the atmospheric boundary layer will comprise the whole domain (from floor to top) the simulation would have to run for a long time if started from uniform inflow conditions. In order to speed-up the simulation, values for u, k and ω are prescribed on all boundaries and the flow field is initialized with these values apriori. The chosen values for the logarithmic BLP are given in Table 1. The shape of the BLP can be adjusted by either changing z_{ref} or z_0. Fig. 10 shows boundary layer profiles for different values of z_{ref} and z_0. Although the chosen velocity profile does not resemble a real atmospheric boundary layer profile it will exemplarily show the effect of wind shear on the turbine. For configuration C only the uniform inflow condition is applied. Before starting the simulation of configuration A or B with a BLP, the same inflow condition is applied to the empty background mesh in order to check if the prescribed velocity profile is a valid solution and if the mesh is suitable for conserving the desired quantities.

C. Results

As stated before at first the convection of the BLP in the empty background mesh is performed. Exemplarily three streamwise (left boundary, middle, right boundary) and three transverse (inflow, middle, outflow) cuts are presented in Fig. 11. The streamwise and transverse velocity profiles are extracted at a height z = 35m above the ground (streamwise: left y-axis, transverse: right y-axis). As can be seen only small velocity deviations occur. The small velocity changes are probably due to the change in numerical dissipation when passing from hexahedral to tetrahedral elements and vice versa.

On the most upper x-axis and most right y-axis the three velocity profiles (inflow, middle, outflow) are depicted as a function of the height above the ground (z). The only noticeable difference occurs at heights between 400 and 500m. The reason for this could not be clarified up to now. Yet the deviations are of minor significance since the region of interest (rotor) is well below this area.

After the verification of the BLP analysis the simulation of the wind turbine will be presented. In this section four different configurations are compared with each other. Configuration A (rotor only) with uniform inflow conditions (A1), configuration A with BLP inflow condition (A2), configuration B (full turbine) with uniform inflow conditions (B1) and configuration B with BLP inflow condition (B2). Fig. 12 shows the comparison of the shaft torque of the different

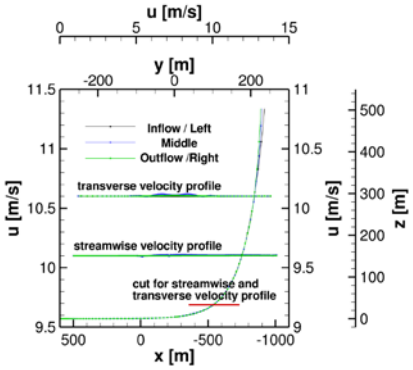

Fig. 11. Development of BLP in empty background mesh.

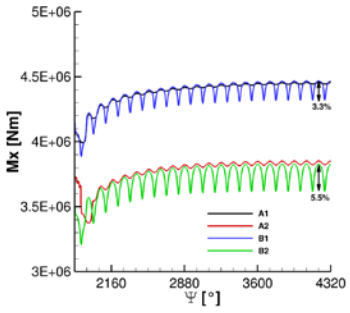

Fig. 12. Shaft torque as function of azimuth for 7 revolutions.

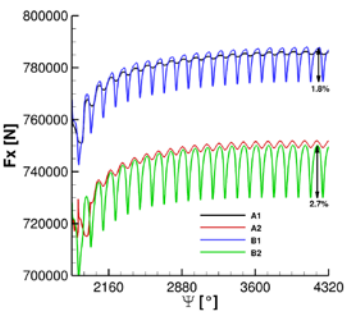

Fig. 13. Thrust as function of azimuth for 7 revolutions.

configurations. The simulations had to be carried out for 12 rotor revolutions in order to reach a satisfactory level of convergence. For clarity reasons Fig. 12 and Fig. 13 only show the last seven rotor revolutions. Two main influences can clearly be seen – the influence of the BLP and the tower shadowing. The influence of the BLP is clearly visible since the average torque of A2 is approximately 14% below the uniform inflow case (A1). The second main influence - the tower shadow – is also very evident in the torque drop every 120°. For the BLP inflow conditions (A2) the torque amplitude roughly reaches 3.3%, while for the full turbine case (B2) the torque amplitude amounts to 5.5%. In the simulation of the uniform inflow conditions (A1) no steady torque output is achieved either. The reasons for that can be found in the non-symmetrical inflow conditions. The sources that most likely contribute the strongest are the shaft and the precone angle. The presence of the ground and the slow development of a boundary layer certainly also add a minor portion to this unsteadiness. Overall though the influence is quite small yielding a torque amplitude of 0.3%. The influence on the unsteadiness due to the BLP is noticeable but small, the torque amplitude for A2 being 0.8%. The same effects can also be seen in the thrust of the various configurations (Fig. 13). The effect of the BLP adds up to an about 4.5% lower thrust force as compared to the uniform inflow case. Compared to the results of Jonkman who reaches a mechanical power output of 5.3 MW the average mechanical power output with BLP (A2, B2) of 4.85 MW is approximately 8.5% below the reference. In the uniform case (A1) the power output is roughly 6% above the reference case (5.62 MW) and for configuration B1 the average mechanical power still exceeds the reference by 5%. The values of the different cases are summarized in Table 2.

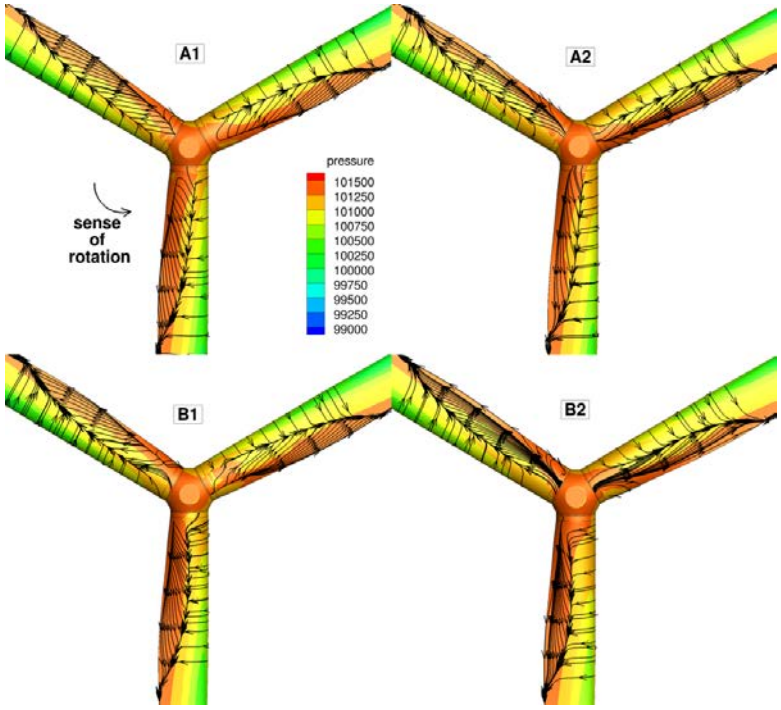

Fig. 14. Surface pressure and streamlines of all configurations.

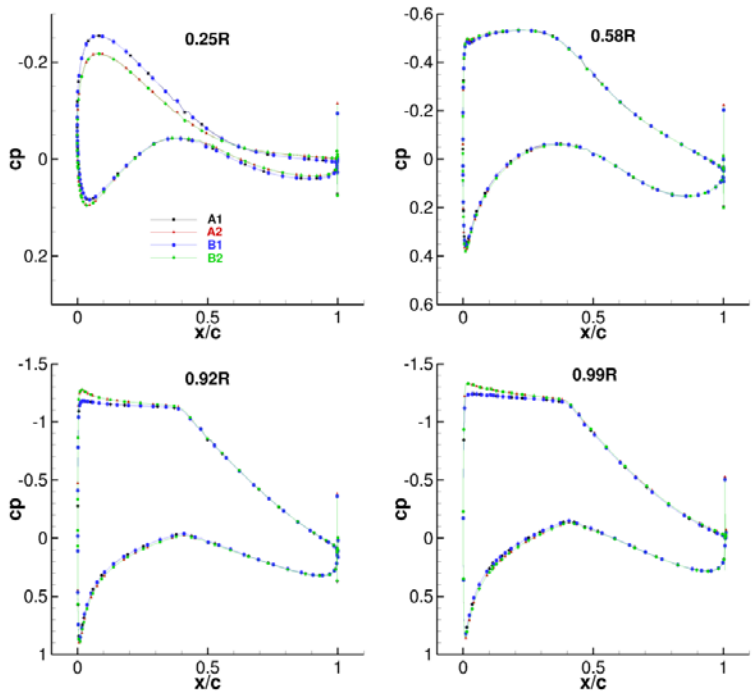

Fig. 15. Pressure coefficients for upper blade.

In Fig. 14 the pressure distribution and the streamlines of the inner part of the rotor of the various configurations is plotted at the time as one blade passes the tower (tower in cases B1 and B2 for visibility reasons not shown). In all cases the flow separation on the inner blade part on the pressure side can clearly be seen. The differences in this 3D graph are hard to see, but the reader might notice that the separation region of the blade passing the tower (B1 and B2) is slightly different in shape than for the other blades. Also the separation region between the cases with uniform and

BLP inflow are slightly different. In the cases with BLP the separation region extends about 0.5m less in radial direction compared to the case with uniform inflow conditions.

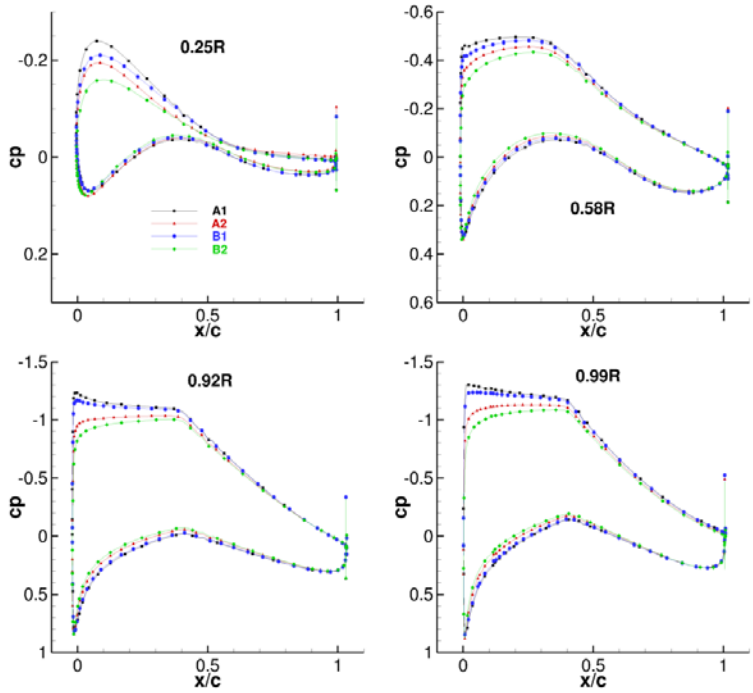

Fig. 16. Pressure coefficients for lower blade passing the tower.

Fig. 15 shows the cp-curves for the blade in 0° position (see Fig.7 for reference) at four different blade stations for the various inflow conditions. No differences can be observed between the cases of alike inflow conditions, i.e. A1 and B1 and between A2 and B2. Moreover the pressure distribution at about midspan (0.58R) of the blade is almost the same for all cases. At the inner part of the blade (0.25R) the inflow velocity for cases A2 and B2 is smaller than for the uniform inflow resulting in a smaller suction peak at this blade section. For the other two blade stations (0.92R and 0.99R) the opposite situation occurs. This is due to the influence of the BLP. In those cases the reference velocity of 11.4 m/s is reached at a height of 100m at the inlet of the flow domain. The increased momentum transport due to the wind shear leads to a decreased flow velocity at the rotor for heights above 100m. Equal flow velocities are reached around midspan of the rotor giving the same pressure distribution and lift coefficients. At higher altitudes the inflow velocity is bigger for configuration A2 and B2 resulting in higher lift forces which can be seen in the increased suction peak for those blade stations.

Table 2. Integral forces on rigid rotor for configuration A, B and C (averaged over last revolution for unsteady cases).

	Configuration A		Configuration B		Configuration C	
	Uniform	BLP	Uniform	BLP	Uniform	Δ_{NREL}
Thrust [kN]	786	750	781	740	780	-1.27 %
Torque [kNm]	4448	3832	4394	3715	4373	+4.12 %

The situation for the lower blade (Fig. 16) is quite different. Here all pressure distributions of the various blade sections differ between each configuration. The highest suction peak for all blade sections is reached for case A1. This result is obvious since the inflow velocity is not decreased by the presence of the BLP nor the tower. The second highest suction peak is achieved by the full turbine configuration in combination with uniform inflow conditions (B1). Here the lift force decreases due to the effect of tower shadowing. The presence of the BLP has a greater effect as can be seen in Fig. 16 since the lift force for the rotor in combination with the BLP (A2) decreases further than for the full turbine with uniform inflow conditions (B1). The lowest pressure coefficient for the blade passing the tower occurs for the full turbine in combination with the presence of the BLP (B2). This is also clear since here the combined effect of tower shadowing and reduced inflow velocity due to the presence

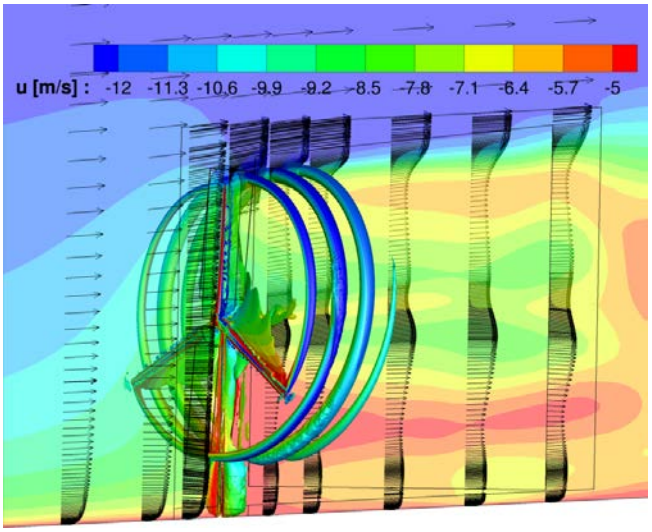

Fig. 17. Flow field around the full turbine (B2), streamwise velocity (u [m/s]), wake using λ2-criterion.

of the BLP come into play. It can also be observed from Fig. 16 that the effect of the BLP becomes greater for the outer blade sections since the difference between B1 and A2 become bigger. This is of course due to the fact that the outer blade sections are closer to the ground and are therefore exposed to lower inflow velocities. In contrary the effect of tower shadowing stays similar for the different blade sections since the difference in suction peak between A1 and B1 is similar for the various blade sections.

The flow field of the complete wind turbine (B2) is presented in Fig. 17 showing the trailing vortices of the rotor by means of the λ_2-criterion. The colour coding indicates the flow velocity in streamwise direction. As can be seen the flow velocity is drastically decreased in the vicinity of the turbine and the wake expands as it travels downstream. The velocity profiles are visualized by the velocity vectors. The BLP in front of the turbine is clearly visible. Interestingly the flow velocities in the proximity of the ground are higher behind the turbine than before. This can be explained by the induced velocities of the tip vortex that increases the streamwise velocity on the outer side of the vortex core and decreases the velocity on the inner side of the tip vortex. This fact is shown in Fig. 17 by the color of the wake structure visualized by $\lambda 2$ - blue on the outside and red on the inside. It can also clearly be seen that most of the energy is extracted on the outer part of the rotor where the streamwise velocity is decreased the strongest.

IV. Aeroelastic Simulation

D. Fluid-Structure-Interaction-Framework

Within the aeroelastic work package of the MERWind project a simulation framework for fluid-structure-interaction (FSI) between the multi-body simulation software SIMPACK and DLR's CFD-code TAU was developed. It allows steady state simulations as well as unsteady simulations in the time domain. The purpose of the framework is to generate high-fidelity loads for the structural design process and to provide data for aeroelastic stability analyses and forced-response investigations.

The FSI-framework as shown in Fig. 18 is integrated into the MERWind-tool chain. Its input consists of the CFD-mesh of the wind turbine and the FE-model of the rotor corresponding to the current design vector. The rotor blade model is imported into SIMPACK as a flexible body including the geometric stiffening effects due to rotations and accelerations. The framework is implemented in Python and relies on DLR's Flow Simulator environment for the information exchange on parallel computing clusters.

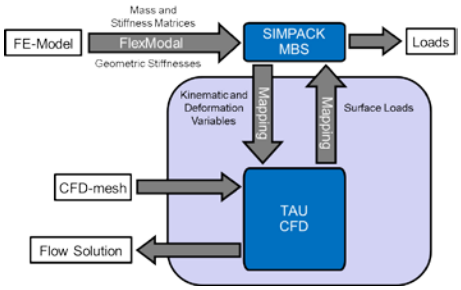

Fig. 18. FSI-Framework.

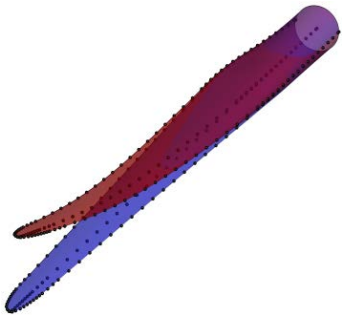

Fig. 19. CFD-surface and structural nodes.

The equations of motion for the flexible wind turbine are solved within the multibody-software, whereas the equations describing the fluid mechanics are solved within the CFD-solver. The task of the FSI-framework therefore consists of transferring rigid-body-motions and surface-deformations from multibody- to CFD-simulation and surface forces in the other direction.

The position of a marker in the multibody-system consists of a rigid-body translation and rotation part superimposed by a flexible body-deformation. In the CFD-solver the rigid body positions and velocities are treated as relative motions of the background grid and any enclosed overset grids. The flexible portion of the position vector is imposed through a deformation of the CFD-grid.

The aerodynamic forces are extracted as surface forces from the CFD-solver and transferred onto the multibody-model. Since the CFD-grid and the multibody-model are discretized differently, an interpolation between the surface nodes of the CFD-grid and the markers of the multibody-model is required.

The spatial interpolation of the deformation from the multibody-system to the CFD-solver is performed by scattered data interpolation based on radial basis functions (a thin plate spline in this case) as described by Beckert and Wendland[16]. A nearest-neighbor-method is implemented for the interpolation of surface forces from the CFD-solver to the multibody-system. First the nearest multibody-marker to each CFD-node k and the vector $\vec{r}$, pointing from marker to node, is determined. The resulting forces $\vec{F}_n$ and moments $\vec{M}_n$ on multibody-marker n are the sum of the contributions of the k CFD-nodes, which the marker is closest to:

$$\vec{F}_n = \sum_k \vec{F}_k, \qquad \vec{M}_n = \sum_k \vec{r}_{nk} \times \vec{F}_k.$$

The coupling for the steady state simulations is performed iteratively with a conventional serial staggered algorithm[17] by alternatingly solving the steady state problem in the CFD- and multibody domains.

E. Computational Setup

The CFD-part of the FSI-computational setup consists of an unstructured cylindrical grid with a radius of $4D$ and a length of $8D$, where $D = 126m$ is the equivalent of the rotor diameter without cone angle. The rotor is positioned $2D$ downstream of the inflow boundary. A structured block is inserted downstream of the rotor to better capture the wake vortices resulting in a total node count of 17.46 million. All FSI-simulations were performed with the 2-equation Menter SST turbulence model in its 2003 version[18].

The multibody-model consists of an isolated rotor on a rigid support without gravitational forces. A rheonomic joint was used to prescribe the rotor speed. The structural and geometric properties of blades and rotor follow the definition of the NREL 5-MW reference wind turbine[13] except for neglecting the tilt angle of the rotor axis, in order to keep the setup rotationally symmetric with respect to the inflow vector.

The rotor blades are modeled with finite element beams in the FEM-tool ANSYS using the same discretization as laid out in the reference document[9]. The FE-model is then imported into the multibody-system as a flexible body taking into account the geometric stiffness effects due to rigid body rotations and accelerations. The first 100 modes of the rotor blades are included in the multibody-simulation.

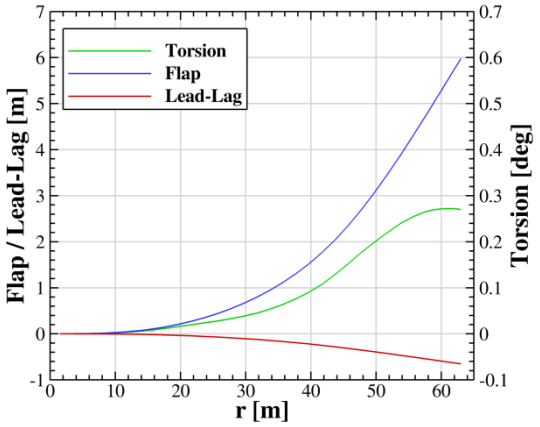

Fig. 20. Radial distribution of the static blade deformations for the rated case.

The spatial interpolation scheme requires additional markers besides the markers on the beam-axis in order to correctly transfer torsional deformations of the structure onto the CFD-mesh. Therefore additional multibody-markers on the leading and trailing edge are inserted and rigidly attached to the beam-axis markers. The resulting distribution of multibody markers relative to the CFD-surface is shown in Fig. 19.

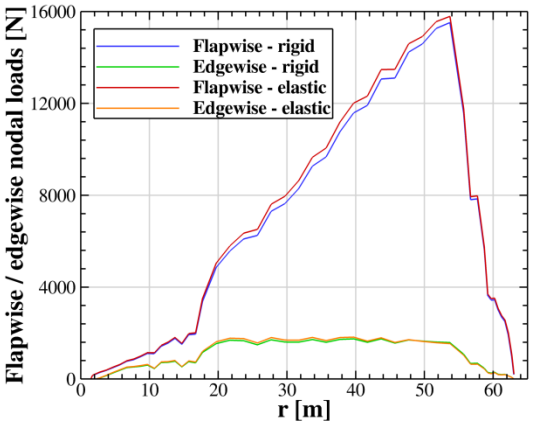

Fig. 21. Flapwise and edgewise loads on the beam axis nodes for the rated case.

The rotor was simulated under rated conditions, which translates into a wind speed of 11.4 m/s and a rotor speed of 12.1 rpm at a blade pitch angle of 0 degrees. The uniform inflow velocity is prescribed through a farfield boundary condition. The rotor rotation is prescribed through grid speeds by coupling the motion of the entire CFD-Mesh to the motion of the rotor hub. Thus it is possible to compute a steady flow solution.

For the rated case a steady flow solution for the undeformed rotor is computed and used for the first deformation of the rotor blades. In following iterations of the coupling algorithm, the structural and flow solutions are exchanged until the static aeroelastic equilibrium between aerodynamic forces and structural deformations is found.

Table 3. Integral forces on the flexible and rigid rotor for configuration C compared to NREL reference values.

	NREL	Rigid		Flexible		
	Absolute	Absolute	Δ_{NREL}	Absolute	Δ_{NREL}	Δ_{Rigid}
Thrust [kN]	790	780	-1.27 %	808	+2.28 %	+3.59 %
Torque [kNm]	4200	4373	+4.12 %	4469	+6.40 %	+2.20 %

F. Static Results

The FSI-process converges within seven steady coupling iterations for the rated case. The maximum difference in deformation between two iterations of any structural degree of freedom is used as a convergence criterion and limited to 10^{-4} m.

In Table 3 thrust and torque from the steady rigid and elastic rotor simulations are listed with reference results from NREL[13]. The rigid simulations overpredict the torque by 4.12 % but slightly underpredict the thrust by 1.27 % relative to the NREL reference values.

Starting from the rigid simulation, the FSI-process predicts a significant flapwise tip deformation of 5.98 m combined with an edgewise tip deformation of 0.65 m. These deformations are displayed along with the wake vortex structure in Fig. 22 and as plots over the blade radius in Fig. 20. The torsional deformation along the blade reaches a maximum of 0.28 degrees at the blade tip. Since the torsional deformation towards larger angles of attack is relatively small, the resulting change in thrust and torque compared to the rigid simulation is also minor with respective increases of 3.59 % and 2.20 %.

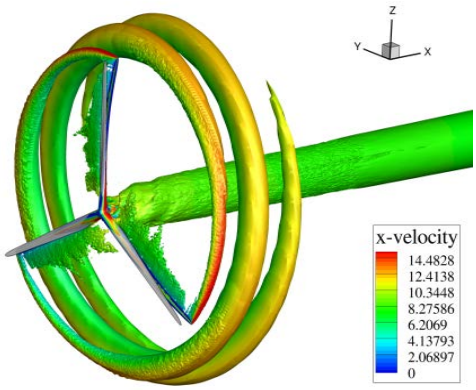

Fig. 22. Wake vortices of the steady, elastic solution for the rated case shown as a $\lambda_2 = -0.02$ isosurface. The rigid rotor is displayed in transparent grey.

The flapwise and edgewise nodal loads on the structure shown in Fig. 21 mirror this behavior. They are larger in the outer part of the rotor blade, where the torsional deformation has an effect. The increase diminishes again, when the influence of the tip vortex sets in.

V. Conclusion

The goals and procedure of the MERWind project have been presented. One of its major innovations is the integral approach that takes into account aspects from the various disciplines. In order to guarantee exceptional quality of the individual simulation tasks employees from four different DLR institutes participate in the project.

In the second part the focus lies on the detailed and time-accurate aerodynamic simulation of the rotor and the complete turbine under uniform and BLP inflow conditions. While those simulations will not be used for the multidisciplinary sensitivity analysis a detailed aerodynamic investigation of the effect of BLP inflow and tower shadowing is done. Moreover these simulations serve as a reference solution for further investigations considering multidisciplinary simulations. The more computationally efficient setup with steady aerodynamic simulations is used in chapter 4. There the FSI-framework intended for the coupled simulations is presented in detail. The successful application of the framework to static wind turbine simulations yielded a first set of results for the NREL-5MW turbine. Static deformations of flap, lead-lag and torsion as well as flapwise and edgewise nodal loads for the elastic and rigid case were presented. The results compare reasonably well with the corresponding reference solution.

Future work will include several wind conditions both for pure aerodynamic and for the coupled computations. Furthermore the support stiffnesses and structures will be included on the aeroelastic side. Another important step will be the automatic generation of the complete FEM model of the blade and its integration in the multidisciplinary design environment. Also the noise prediction of the reference blade and a modified design using CAA is envisioned for the end of the project. While on one side aeroelastic and -acoustic simulations with a high degree of detail will be carried out for hand selected designs to understand the involved physical phenomena, a simplified setup will be defined which allows to overcome the shortcomings of traditional low-fidelity models, e.g. blade element momentum theory, at reasonable turn-around times.

References

[1]M. O. L. Hansen, J. N. Sørensen, S. Voutsinas, N. Sørensen, H. Aa. Madsen, *"State of the art in wind turbine aerodynamics and aeroelasticity"*, Progress in Aerospace Sciences, Vol. 42, 285-330, 2006.

[2]Sørensen, N. N., Michelsen, J. A. and Schreck, S. (2002), *"Navier–Stokes predictions of the NREL phase VI rotor in the NASA Ames 80 ft × 120 ft wind tunnel"*. Wind Energ., 5: 151–169.

[3]N. N. Sørensen and J. Johansen, *"UPWIND, aerodynamics and aero-elasticity: rotor aerodynamics in atmospheric shear flow"*. European Wind Energy Conference, Milan, Italy, 7-10 May 2007.

[4]K. Meister, Th. Lutz, E. Krämer, *"Consideration of unsteady inflow conditions in wind turbine CFD Simulations"*, DEWEK 2010, Bremen.

[5]N. Troldborg, F. Zahle, P.-E. Réthoré, N. N. Sørensen, *"Comparison of the wake of different types of wind turbine CFD models"*, 50th AIAA Aerospace Sciences Meeting, 09-12 January 2012, Nashville, Tennessee.

[6]D. Schwamborn, T. Gerhold and R. Heinrich, *"The DLR TAU-Code: Recent Applications in Research and Industry"*, In proceedings of "European Conference on Computational Fluid Dynamics" ECCOMAS CDF 2006, Delft The Netherland, 2006.

[7]S. Freund, F. Heinecke, T. Führer and C. Willberg, *„Parametric Model Generation and Sizing of Lightweight Structures for a Multidisciplinary Design Process"*, NAFEMS, 20-21 May in Bamberg Germany.

[8]J. Arnold, *"Using multibody dynamics for the simulation of flexible rotor blades - Getting the mechanical coupling right?"*, 35th European Rotorcraft Forum, 22-25 September 2009, Hamburg, Germany.

[9]U. Siller, C. Voss and E. Nicke, *"Automated multidisciplinary optimization of a transonic axial compressor"*, AIAA Aerospace Sciences Meeting 2009, Orlando, USA AIAA2009-863.

[10]C. Liersch and M. Hepperle, *„A distributed toolbox for multidisciplinary preliminary aircraft design"*, CEAS Aeronautical Journal, 2, pp. 57-68, December 2011.

[11]R. Ewert, J. Dierke, J. Siebert, A. Neifeld, C. Appel, M. Siefert and O. Kornow, *"CAA broadband noise prediction for aeroacoustic design"*, 2011, Journal of Sound and Vibration, 330(17), pp. 4139-4160.

[12]T. Schwarz, *"The Overlapping Grid Technique for the Time Accurate Simulation of Rotorcraft Flows"*, 31st European Rotorcraft Forum, Florenz, Italien, 13. – 15. September, 2005.

[13]J. Jonkman, S. Butterfield, W. Musial and G. Scott, "*Definition of a 5-MW reference wind turbine for offshore system development*", NREL/TP-500-38060, 2009.

[14]X. Zhang, "*CFD simulation of neutral ABL flows*", Technical Report, Risø National Laboratory, Roskilde, 2009.

[15]T. Knopp, B. Eisfeld, J. Bartolome Calvo, *"A new extension for k-ω turbulence models to account for wall roughness"*, International Journal of Heat and Fluid Flow, Vol. 30, p. 54-65, 2009.

[16]A. Beckert and H. Wendland, "*Multivariate interpolation for fluid–structure-interaction problems using radial basis function,*." Aerospace Science andTechnology 5125, 2001.

[17]C. Farhat and M. Lesoinne, *"Fast staggered algorithms for the solution of three-dimensional nonlinear aeroelastic problems"*, AGARD SMP Meeting on Numerical Unsteady Aerodynamic and Aeroelastic Simulation (R-822).

[18]F. R. Menter, M. Kuntz and R. Langtry, *"Ten Years of Industrial Experience with the SST Turbulence Model"*, Turbulence, Heat and Mass Transfer 4, ed: K. Hanjalic, Y. Nagano, and M. Tummers, Begell House, Inc., 2003, pp. 625 - 632.

[19]D. O. Yu, O. J. Kwon,"Predicting wind turbine blade loads and aeroelastic response using a coupled CFD-CSD method, Journal of Renewable Energy, Vol. 70, p. 184-196, 2014.